Color-Selective 2.5D Holograms on Large-Area Flexible Substrates for Sensing and Multilevel Security

Ali K. Yetisen, Haider Butt, Tatsiana Mikulchyk, Rajib Ahmed, Yunuen Montelongo, Matjaž Humar, Nan Jiang, Suzanne Martin, Izabela Naydenova, and Seok Hyun Yun**

2.5D photonic nanostructures with narrow-band diffraction characteristics have a vast range of potential applications in information storage, tunable lasers, optical filters, and biosensors. However, fabrication of 2.5D photonic devices over large areas remains expertise-dependent, inaccurate, and high-cost, limiting their widespread use in practical applications and consumer products. Here, large area printing of quasi 2.5D holograms is demonstrated in the visible spectrum. These holographic surface-relief gratings are hexagonally packed lateral microscale honeycomb pyramids consisting of vertical nanoscale steps. The consecutive steps act as Bragg gratings producing constructive interference of selective visible wavelengths. The 2.5D nanostepped pyramids exhibit coloration due to the narrow-band Bragg diffraction that is tuned in the visible spectrum and a wide angular range. Roll-to-roll processing allows for rapid nanoimprinting the 2.5D nanostepped pyramid arrays over large areas of acrylate polymer film on poly(ethylene terephthalate) substrate. The utilities of the 2.5D holograms are demonstrated by creating colorimetric refractive index and relative humidity sensors, quick response codes, fingerprints, signatures, and encrypted labels. It is envisioned that 2.5D holograms can be integrated with desktop dot-matrix printers for application in sensing, data storage, and security.

1. Introduction

Photonic nanostructures operating from ultraviolet to near-infrared regions have applications in tunable lasers, light trapping, optical filters, data storage, dynamic displays, and biosensors.[1,2] Photonic devices have been fabricated by self-assembly and microfabrication, or combination of both.[3] Bottom-up fabricated periodic optical nanostructures include crystalline colloidal arrays,[4] inverse opals,[5] block copolymer gratings,[6] and Bragg stacks.[7] However, photonic structures obtained by self-assembly methods are prone to defects; therefore, the mass production of uniform, defect-free, large-area 3D photonic structures, in particular with narrow-band diffraction in the visible spectrum is limited.[8] For example, producing high-quality monodisperse, highly-charged polystyrene particles through emulsion polymerization to prepare opals require lengthy dialysis times (hours to days), limiting their potential for practical applications.[1] Other self-assembly approaches including layer-by-layer deposition and spin coating suffer from layer instability and time-consuming fabrication processes. Top-down approaches such as electron beam lithography,[9] focused ion beam milling,[10] multidirectional etching,[11] and laser lithography[12] of single-crystalline semiconductors or dielectric materials allow direct creation of high-quality 3D photonic structures. Silicon, gallium arsenide, and tungsten have been incorporated into 3D templates via chemical vapor deposition, followed by removal at a later stage.[13] Direct fabrication of 3D photonic crystals (PCs) was also demonstrated through layer-by-layer assembly involving multiple lithographic writing and etching steps.[14] However, these approaches require wafer fusion for

Dr. A. K. Yetisen, Dr. M. Humar, Prof. S. H. Yun
Harvard Medical School and Wellman Center for Photomedicine
Massachusetts General Hospital
65 Landsdowne Street, Cambridge, MA 02139, USA
E-mail: ayetisen@mgh.harvard.edu; syun@mgh.harvard.edu

Dr. A. K. Yetisen, Dr. M. Humar, Dr. N. Jiang, Prof. S. H. Yun
Harvard-MIT Division of Health Sciences and Technology
Massachusetts Institute of Technology
Cambridge, MA 02139, USA

Dr. H. Butt, R. Ahmed
Nanotechnology Laboratory
School of Engineering
University of Birmingham
Birmingham B15 2TT, UK

T. Mikulchyk, Dr. S. Martin, Dr. I. Naydenova
Centre for Industrial and Engineering Optics
School of Physics
College of Sciences and Health
Dublin Institute of Technology
Kevin Street, Dublin 8, Ireland

Dr. Y. Montelongo
Department of Chemistry
Imperial College London
South Kensington Campus
London SW7 2AZ, UK

Dr. M. Humar
Condensed Matter Department
J. Stefan Institute
Jamova 39, SI-1000, Slovenia

DOI: 10.1002/adom.201600162

each layer and accurate alignment of the setup. Furthermore, 3D PC woodpile structures with a complete gap of 3.5% have been fabricated by direct laser writing in chalcogenide glasses in 2 h.[12] 3D photonic nanostructures operating at near-infrared and longer wavelengths larger than 100 μm × 100 μm × 100 μm with uniformity have been fabricated via laser lithography.[15] However, these 3D nanostructures typically have periodicities of the order of several microns that display photonic bandgaps beyond the visible range. 3D structures cannot be mass produced through embossing or roll-to-roll printing. Additionally, 2.5D photonic structures have also emerged as a major extension of 2D planar semiconductor technologies with an added third vertical dimension using multilayer stacks.[16] In these structures, lateral index contrast is combined with a 1D vertical high-index contrast.[17] Analogous to their 3D counterparts, 2.5D structures are fabricated by molecular beam epitaxy, chemical vapor deposition, electron beam lithography, wet chemical etching, and wafer bonding.[18] Therefore, a technique to accurately print color-selective 2.5D photonic nanostructures on flexible substrates in a single step at industrial production speeds is desirable.

Denisyuk's work on reflection holograms in the 1960s has led to imaging 3D objects using laser light.[19] Denisyuk holography involves recording a latent image of scattered light from an object in a light-sensitive recording medium via silver halide chemistry or dichromated gelatin.[20] The recorded latent image can be amplified by photographic developers or application of heat. When illuminated with broadband light, reflection holograms diffract narrow-band (monochromatic) light.[21] The lattice spacing and the Bragg peak of the diffracted light can be controlled by changing the wavelength of laser light that was used to record the hologram or swelling/shrinking the recording medium to create pseudocolors.[22] These structures cannot be multiplied by embossing. Holography can also be configured to operate in transmission mode to image 3D objects. This method, known as off-axis Leith–Upatnieks holography, requires a monochromatic light source to replay recorded image.[23] Gratings recorded in photoresist films can be used to produce a metal master hologram that can be embossed on a surface.[24] These gratings (Benton holograms) diffract rainbow colors when illuminated with broadband light.

Here, we demonstrate the development and optical characterization of large area printing of quasi 2.5D photonic structures in the visible spectrum and show their application in sensors and displays. These structures are hexagonally packed lateral microscale pyramids consisting of vertical nanoscale steps. The consecutive steps act as Bragg gratings producing constructive interference of selective visible wavelengths. In our strategy, we combine prism coupling interference and off-axis Leith–Upatnieks holography to create printable 2.5D photonic nanostructures. Analogous to volume holograms, the present technology also provides tunability of the diffraction in the visible spectrum. The present work demonstrates open 2.5D surface relief patterns to print Bragg gratings. This strategy allows for scalable printing of uniform color-selective 2.5D photonic structures at low cost. These photonic structures can be printed on flexible polymer substrates in roll-to-roll manufacturing. We show the utilities of the 2.5D structures by creating colorimetric refractive index and relative humidity sensors, and multilevel security labels with encrypted information.

2. Results and Discussion

2.1. Design and Optimization of 2.5D Nanostepped Pyramids

The 2.5D photonic structures comprise of a honeycomb array with circular convex step-variable gratings, resembling Teuchitlan pyramids (Guachimontones, Mexico) (**Figure 1**a). These structures show narrow-band colors due to nanosteps.[25] The hexagonal array of circular hollow pyramids was designed to have a pitch of 3.3 μm and an apex-base distance of ≈1.1 μm. The pyramids consist of 5–6 nanosteps, with a variable step height (h) from 160 (h_1) to 200 nm (h_2), and a step width of 250 nm. The pyramids are made of acrylate polymer (AP) (n ≈ 1.49) on poly(ethylene terephthalate) (PET) film (n ≈ 1.57), and their inner surface has an aluminum coating (20 nm, $n = 1.09 + i6.79$). Prior to fabrication, the optical properties of thin layer of the honeycomb array of nanostepped pyramids were analyzed by computational modeling. The interaction of the electromagnetic field with the nanostepped pyramids was modeled by finite element method within a hemisphere boundary using COMSOL Multiphysics (Figure 1b). Experimental Section "Modeling of the Honeycomb Nanostepped Pyramids" describes the parameters of the model. The light wave propagation at a normal incidence was computed for nanostepped pyramids with different step sizes ranging from 160 to 200 nm. Figure 1c–e illustrates the electromagnetic field distributions within the hemisphere screen for the modeled geometries with step heights of 160, 180, and 200 nm while keeping the step width constant at 250 nm.

The blue resonance of the diffracted light (496 nm) is focused near zero order (Figure 1c), whereas for red resonance (612 nm), the diffracted light diverges from the zero order (Figure 1e). As the step height increased from 160 to 200 nm; the central wavelength of the narrow-band reflected light shifted from 496 to 612 nm (Figure 1f). Thus, varying the step height allowed for tuning the color of the grating throughout the visible spectrum. Bragg peak was narrow band due to the periodicity in the vertical direction. The shift in the position of the Bragg peak with increasing step height had a linear trend (Figure 1g). The full width at half maximum (FWHM) of the simulated structures broadened from 38 to 74 nm with increasing step height as the total height of the pyramids was kept constant (Figure 1g inset). Additionally, the diffraction efficiency of the Bragg peak could be controlled by changing the number of steps in the pyramids. The reflection of the gratings increased from 40% to 95% as the number of steps increased from 4 to 12 (Figure 1h). The inset in Figure 1h shows the enhancement in the reflection of the simulated spectra for 4, 8, and 12 steps, and bandwidth narrowing with increasing step number.

2.2. Laser Writing of Holographic 2.5D Nanostructures

The photonic nanostepped pyramids were fabricated by multibeam holographic lithography and subsequently nanoimprinted

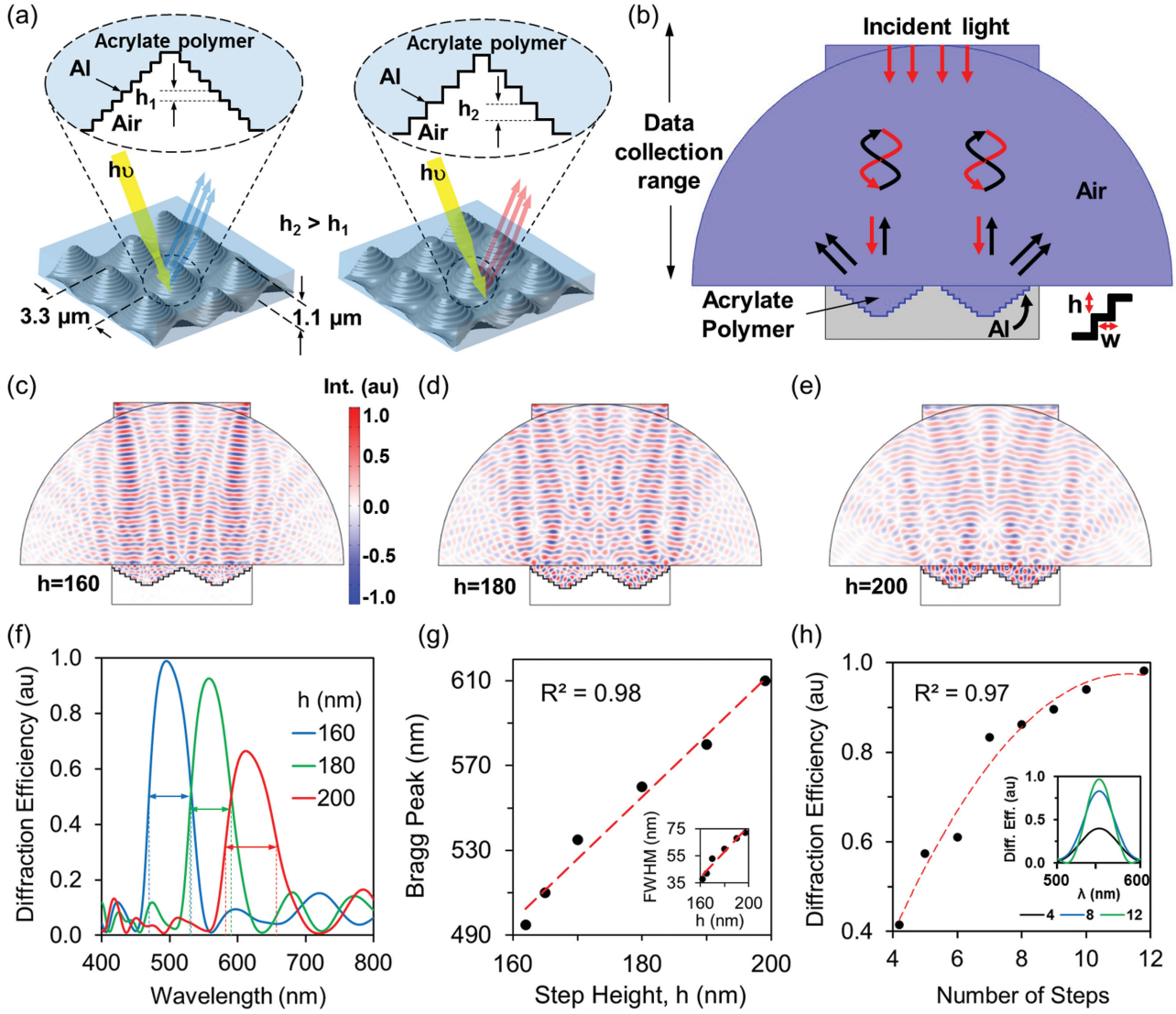

Figure 1. Honeycomb array of the circular nanostepped pyramids. a) The principle of operation of the photonic device showing a shift in the diffracted light from blue to red as the step height is increased. b) Simulated model in a hemisphere boundary. Pyramid height was 1.1 μm with a pitch of 3.3 μm, and the overall width and height of the modeled grating was 8 and 2 μm, respectively. The step width was kept constant at 250 nm. Simulated models of the diffracted light at c) 496, d) 558, and e) 612 nm show the interaction of the electromagnetic waves with the nanostepped pyramids. f) The positions of the modeled Bragg peaks as a function of the step size at 160, 180, and 200 nm. g) Bragg peak position with increasing step height. The inset shows broadening FWHM as a function of step height. h) Reflection as a function of step number. The inset illustrates the diffraction efficiency of pyramids (h = 180 nm) with 4, 8, and 12 steps at 530 nm.

with AP on PET film. The pyramidal pattern was obtained by superposing multilayer and honeycomb exposure fields in a positive photoresist layer (diazonaphthoquinone, thickness = 1.2 μm, n = 1.65). First, the holographic interference pattern coplanar with the photoresist surface (Ø = 14 cm) was photochemically patterned using prism coupling (**Figure 2**a). To create multilayer exposure, a triangular gadolinium gallium garnet prism (n = 1.97) was aligned over the photoresist layer, where the refractive index was matched by xylene (n = 1.49). The total internal reflection of a coherent argon ion laser beam (λ = 458 nm) from the photoresist–air interface for 1 min created the multilayer interference pattern. By increasing the angle of incidence normal at the prism surface plane from 30° to 44°, the vertical lattice step height of the multilayer pattern was tuned from 160 to 200 nm at different regions of the photoresist. To create hexagonally packed cylindrical interference fringes running normal to the photoresist surface plane, three azimuthal beams (α = 120°) were interfered in the photoresist layer to create a pitch (w) of 3.3 μm (Figure 2b). The resulting structure is a superposition of multilayer and honeycomb interference patterns consisting of circular concavities (Figure 2c). After the photographic development of the photoresist, the intensity variations were translated into nanostepped pyramids (Figure 2d). "Holographic Recording of the Honeycomb Nanostepped Concavities" in the Experimental Section demonstrates step-by-step fabrication of the devices.

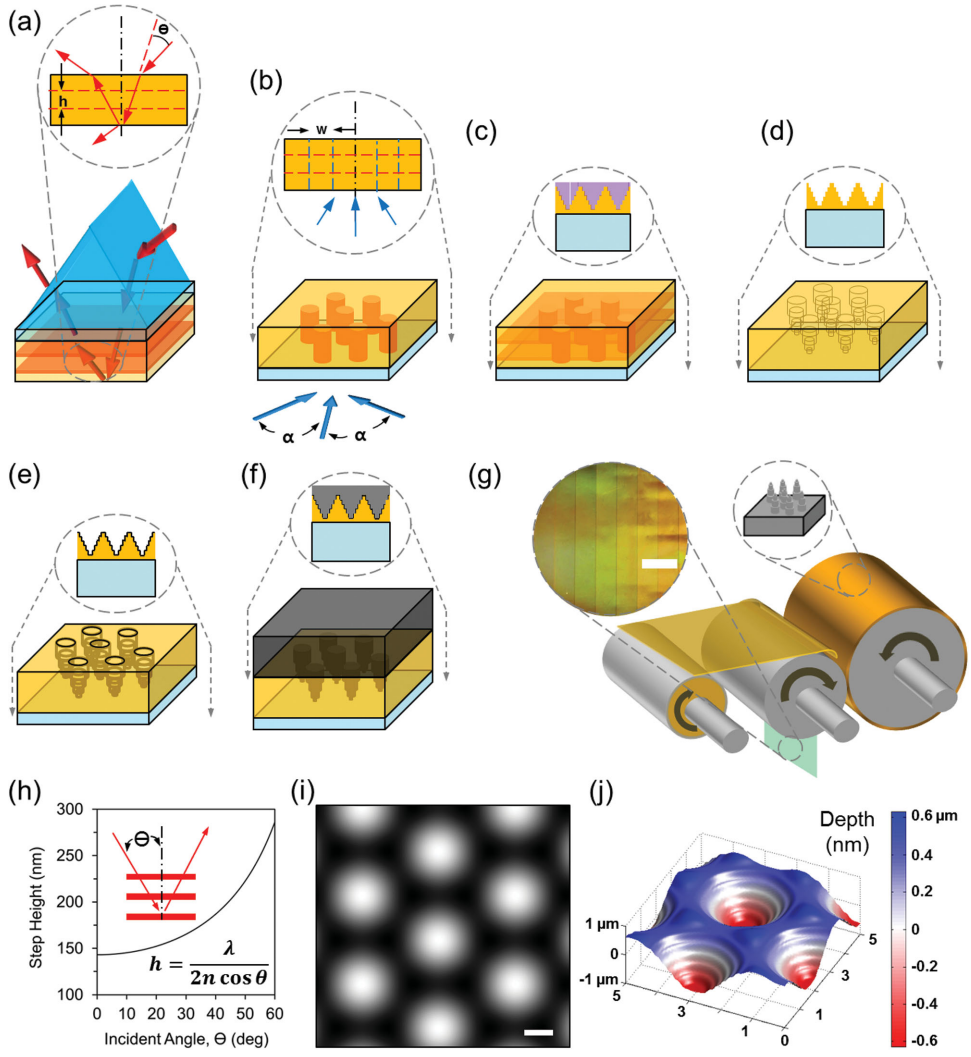

Figure 2. Holographic recording and printing of circular nanostepped pyramids in honeycomb arrays. a) Prism coupling to expose a multilayer interference field in a photoresist layer coated over glass. b) Laser writing of a honeycomb pattern using three azimuthal beams ($\alpha = 120°$) to create a pitch (w) of 3.3 μm. c) Resulting interference, a superposition of the multilayer and the honeycomb pattern, shown in purple. d) Circular nanostepped pyramids after etching with a photographic developer. e) Evaporation of a silver layer (≈300 nm) over the etched photoresist in vacuum. f) Electroplating metallic nickel (1 mm) over the deposited silver layer to produce a master. g) Printing the nanostepped pyramids using a nickel replica into AP on PET film in roll-to-roll nanoimprinting. The inset shows eight different printed gratings, scale bar = 4 cm. h) The vertical lattice step height of the multilayer as a function of incident angle (θ) in prism coupling. i) Simulated honeycomb field intensity using three azimuthal beams ($\alpha = 120°$) in the photoresist. Scale bar = 1 μm. j) The modeled nanostepped concavities computed by superposing the multilayer and the honeycomb exposures.

To print the 2.5D photonic structure on flexible substrates, an inverse master was produced. A silver layer (300 nm) was deposited over the photoresist to form a conductive layer (Figure 2e), thus allowing for electroplating of nickel metal over the concavities (Figure 2f). The nickel master (14 × 14 cm^2, t = 1 mm) consisting of convex stepped pyramids was installed onto a cylindrical drum of a roller-type replication machine, and the AP pyramids were nanoimprinted onto a PET film (50 μm) (Figure 2g).[26,27] The inset in Figure 2g shows the imprinted film consisting of stripes with different nanostep heights in the visible spectrum. To increase the diffraction efficiency, an aluminum layer (20 nm) was coated over the concavities. AP nanostepped pyramids were printed over 1 m^2 of PET film within a minute via roll-to-roll manufacturing, allowing a scalable production of gratings on large surface areas. The resulting structures were instantaneously usable as narrowband Bragg gratings with peaks in the visible spectrum. The step-by-step fabrication is described in the Experimental Section "Printing Bragg Gratings in Roll-to-Roll Manufacturing."

To predict the interference patterns which produced the multilayer and the honeycomb pattern in the photoresist, laser light interference arising from superposition of multiple light waves was modeled. The creation of the nanostructure was simulated for multilayer interference in prism coupling, and off-axis Leith–Upatnieks interference.[28] The interference pattern was created by two main waves: (1) the incident beam to the photoresist, and (2) the beam reflected internally at the photoresist-substrate–air interface during prism coupling exposure.

Figure 2h shows the lattice spacing of the multilayer as a function of incidence angle in prism coupling. The vertical lattice spacing is

$$h = \frac{\lambda}{2n\cos\theta} \tag{1}$$

where λ is the wavelength of the laser light, n is the refractive index of the photoresist, and θ is the incident angle measured with respect to the normal to the prism surface plane. Equation (1) shows the principle of prism coupling recording, obeying Bragg's law. Increasing θ from 10° to 60° allows for tuning the step height from 150 to 275 nm. The off-axis Leith–Upatnieks interference was modeled by calculating the superposition of three azimuthal beams. To retrieve the honeycomb exposure, the interference of three wave fronts was computed as

$$E_1(r,t) = Ae^{i\left(\frac{2\pi n}{\lambda}(x\sin(\alpha)+z\cos(\alpha))-\omega t+\phi_1\right)} \tag{2}$$

$$E_2(r,t) = Ae^{i\left(\frac{2\pi n}{\lambda}\left(\frac{-x\sin(\alpha)}{2}+\frac{y\sqrt{3}\cos(\alpha)}{2}+z\cos(\alpha)\right)-\omega t+\phi_2\right)} \tag{3}$$

$$E_3(r,t) = Ae^{i\left(\frac{2\pi n}{\lambda}\left(\frac{-x\sin(\alpha)}{2}-\frac{y\sqrt{3}\cos(\alpha)}{2}+z\cos(\alpha)\right)-\omega t+\phi_3\right)} \tag{4}$$

where $E(r,t)$ is the electric vector, A is the wave amplitude, ω is the angular frequency, and ϕ is the phase of the plane waves. The three wave vectors are defined with a polar angle from the normal α and azimuthal angles of 0°, 120°, and 240°. The waves constructively and destructively interfere in the photoresist producing an intensity distribution

$$\langle I(r)\rangle = \int_0^t \left|E_1(r,t)+E_2(r,t)+E_3(r,t)\right|^2 dt \propto \left|E_1(r)+E_2(r)+E_3(r)\right|^2 \tag{5}$$

To visualize the intensity distribution, the electromagnetic field in every point over 10 × 10 μm^2 in the photoresist surface plane was evaluated. Through computing the respective intensities and phases of individual plane waves, an interference pattern was extracted (Figure 2i). White (high intensity) and black regions represent the spatial variation of light intensity for the photoresist exposure. This exposure creates a honeycomb interference pattern that runs perpendicular to the surface plane of the photoresist. Superposing the multilayer interference and the off-axis Leith–Upatnieks interference produces a circular nanostepped pyramid. Figure 2j shows the 3D intensity distribution of the superposed fields in a medium, where the pitch of the honeycomb is 3.3 μm, and the depth of a nanostepped pyramid is 1.1 μm.

2.3. Microscopic Analyses of the Holographic Nanosteps

Figure 3a illustrates scanning electron microscope (SEM) images of a honeycomb array produced with an incident angle θ of 40° during prism coupling (Experimental Section "SEM Protocol"). The inset in Figure 3a shows a single concavity with 6 steps. The SEM images of the vertical cross-section of the sample show that circular concavities have uniform step profiles (Figure 3b). The number of steps of the concavities decreased from 6 to 5 as the incident angle θ was increased from 30° to 44° during prism coupling. Figure 3c shows atomic force microscope (AFM) 3D surface topography of the honeycomb array within 5 × 5 × 2 μm^3 (Experimental Section "AFM Protocol"). Figure S1 of the Supporting Information shows reproducibility of the array at large dimensions. The pitch of the concavities in the honeycomb array was 3.3 μm, and a single concavity had a step height ranging from ≈160 to ≈200 nm, respectively (Figure 3d). The step width was ≈250 nm in all samples. The concavity distribution and the surface topography of the structures can be accurately predicted by prism coupling and off-axis Leith–Upatnieks interference models (Equations (1)–(5)).

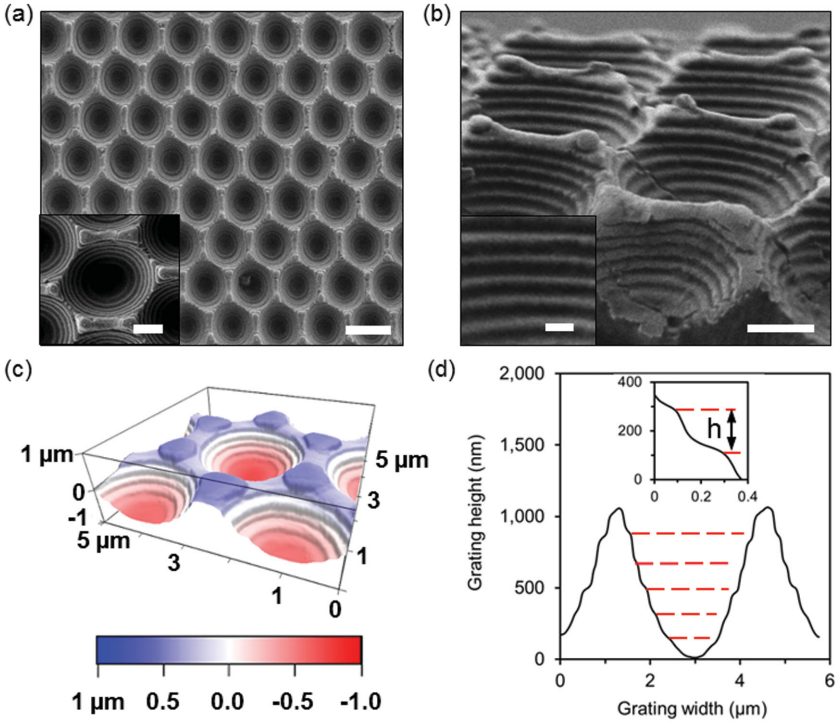

Figure 3. Microscopic analyses of the 2.5D nanosteps in honeycomb array. a) SEM image of the array shows uniform distribution of circular concavities. Scale bar = 3 μm. The inset shows a single concavity, Inset scale bar = 1 μm, b) A concavity with six steps. Scale bar = 1 μm. The inset shows individual steps. Inset scale bar = 200 nm. c) AFM surface topography of the array illustrates nanostepped concavities. d) Measured concavity step height is ≈190 nm. The inset shows a single step with 200 nm width.

2.4. Optical Characterization of Holographic Nanostructures

Figure 4a shows the photographs of the honeycomb array viewed from normal to the PET side. Changing the incident angle from 30° to 44° with 2° increments during prism coupling increased the step height of the pyramids from 160 to 200 nm. This tuning mechanism allowed for shifting the diffracted light by 2.8 nm per degree in the entire visible spectrum. The holographic array was illuminated vertically by a laser beam ($\lambda = 532$ nm), and the back scattered light was projected on the screen of a semitransparent hemisphere screen. Under monochromatic illumination, the array diffracted multiple orders in hexagonal spots (Figure 4b). The 1st, 2nd, 3rd, and 4th diffracted orders were measured at approximately 10°, 21°, 30°, and 40° due to the periodicity of the hexagonal pattern. Figure 4c–e shows the diffracted light from three different honeycomb arrays with nanostepped pyramids comprising step heights of approximately 160, 180, and 200 nm, respectively. When illuminated with fiber optic diffused broadband light at incident angle, the photonic structure diffracted light over the hemisphere screen up to 20° from the normal. Additionally, the grating diffracted violet light (blue and red colors) at angles higher than 20° under diffuse light illumination.

The spectra of the Bragg peaks were measured using an optical fiber coupled into a port of an upright optical microscope. The Bragg peaks of the holographic array with pyramid step heights ranging from 160 to 200 nm were studied at normal incidence. Figure 4f shows the photonic band gaps of the pyramids with the step heights of 160, 180, 200 nm, blue, green, and red lines, respectively. The spectral bandwidths of the Bragg peaks increased as the step height increased from 160 to 200 nm. The bandwidths were approximately equal to the reciprocal of the number of steps. Figure S2 of the Supporting Information shows Bragg peaks of eight different arrays. To measure the diffraction efficiency, the nanostepped pyramids were illuminated approximately normal to the surface plane either with 491, 532, and 640 nm laser beams. The diffracted light from individual diffraction spots were measured with an optical power meter. The maximum diffraction efficiency was calculated by adding the diffraction efficiencies of the first three orders in the hexagonal pattern. When illuminated with 491, 532, and 650 nm light, gratings with step sizes of 160, 180, and 200 nm had the maximum efficiencies of 15.5%, 10.6%, and 6.8%, respectively. The decrease in the diffraction efficiency with increasing step height can be attributed to the decrease in the number of steps as the thickness of the photoresist was constant. Figure S3 of the Supporting Information shows the first

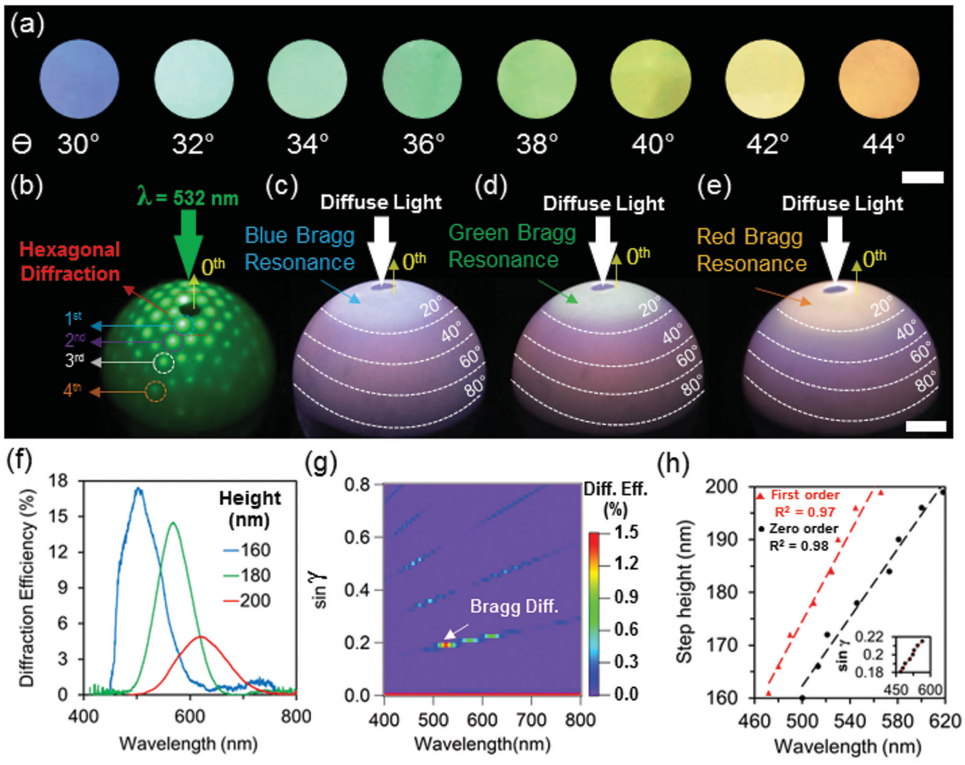

Figure 4. Optical characterization of the holographic honeycomb array consisting of 2.5D nanostepped pyramids. a) Photographs of eight different gratings produced by increasing the incident angles during prism coupling from 30° to 44°, and subsequent off-axis Leith–Upatnieks patterning. Scale bar = 1 cm. b) Monochromatic hexagonal light diffraction from a honeycomb array in a hemisphere screen photographed at 60° from the normal. c) Blue, d) green, and e) red resonances of the arrays with step heights of 160, 180, and 200 nm under diffuse light illumination, showing isotropic color distribution below 20° from the normal, photographed at 80° from the normal. The pyramidal array was leveled at the bottom of the hemisphere. f) Bragg peaks of the nanostepped pyramids (h = 160–200 nm) as a function of step height at normal incidence in the visible spectrum. g) Angle-resolved spectral measurements of an array with a step height of ≈200 nm. h) Zero and first order Bragg peak positions of the nanostepped pyramids as a function of step height. The inset shows angular dependence (160–200 nm).

order diffraction efficiencies of the nanostepped pyramids. To resolve the angular diffraction, a 3 mm spot on the stepped pyramids was illuminated at normal incidence with a broadband light source. The backscattered light was spectrally analyzed at 1° increments from 0° to 60° relative to the sample normal using a spectrometer positioned on a robotic goniometer. Figure 4g illustrates the angle-resolved spectra of pyramids with step height of 190 nm for different collection angles as a function of diffraction intensity. The normal incidence Bragg peak at 530 nm (indicated by an arrow in Figure 4g) was visible in all of the higher-order diffraction modes following an arc-shaped pattern as predicted by Bragg's law for changing incidence angle. The Bragg grating diffracted narrow-band light at ≈10° from normal with an efficiency of 1.4% measured for a single 1st order diffraction spot in the blue/green region (≈520 nm). The nanostepped pyramids Bragg-diffracted the light analogous to a multilayer reflection grating. Figure 4g shows the diffraction angle; the coherent scattering of the Bragg multilayer peak and a surface grating superposed to create a hierarchical optical characteristic of the photonic structure. There were also minor increases in the intensity of non-Bragg regions. This feature could be caused by the parabolic nature of the concavity depressions, variation in step height or thickness of the sample. The parabolic depression profile of the step height may be attributed to the nonlinear etching of photoresist due to the decrease in the concentration of developer or desensitization of the surface. Figure 4h illustrates the zero and first order Bragg peak positions as a function of step height. As the step height increased from 160 to 200 nm, the zero and first order Bragg peaks red shifted by 120 and 100 nm, respectively. The direction of the first diffracted light was ≈10° from the normal (Figure 4h inset). "Optical Characterization" in the Experimental Section describes measurement devices and techniques.

2.5. Refractive Index Sensing

To demonstrate the utility of the 2.5D holographic arrays, we show an application in sensing. The Bragg peak of the diffracted light from the nanostepped pyramids is affected by changes in the refractive index of the surrounding medium. This feature can be used as a colorimetric refractive index sensor to quantify the concentration of analytes. Finite element method simulations show that as the refractive index of the surrounding medium was increased from 1.33 to 1.47, the Bragg peak shifted from 493 to 532 nm, respectively (**Figure 5**a). Figure S4 of the Supporting Information illustrates Bragg peaks for eight different simulated refractive index values. Glycerol was utilized as a model sensing analyte. Glycerol is a caloric macronutrient, and its measurement in water has applications in pharmaceuticals and food industry. As the surrounding medium of the grating was incrementally changed from deionized water to increasing concentrations of glycerol, the Bragg peak shifted from 495 to 535 nm (Figure 5b). In contrast to the simulated spectra in Figure 5a, the experimental Bragg peak response exhibited negligible side lobes as the number of nanostepped pyramids was significantly higher than the simulated structure. The Bragg peak followed a linear shift as the concentration of glycerol was increased from 10 to 100 vol % corresponding to a refractive index change from 1.346 to 1.472, respectively (Figure 5c). The experimental readouts agree with a handheld refractometer and simulated Bragg peaks, allowing the prediction of the refractive index of glycerol using computational modeling. The sensitivity of the sensor was 0.00104 refractive index units (R^2 = 0.99) corresponding to a concentration of 0.75 (vol%) using a spectrophotometer with 0.3 nm resolution. The sensitivity of the sensor may improve with increasing spectrophotometer resolution. The colorimetric results were visible to the eye within seconds of changing the concentration of the glycerol (Figure 5d). The sensors showed inter-assay reproducibility from batch to batch (n = 10), and no hysteresis and Bragg peak broadening were recorded; hence, the same sensor can be used for repeat measurements. Recently, aluminum nanoclusters with plasmonic Fano resonances,[29] 2D silicon nanowire arrays,[30] and porous mixed metal oxide-TiO_2 1D photonic crystals.[31] have been reported for colorimetric refractive index sensing. In addition to the comparable sensitivity with the reported sensors, the present holographic technology has the added advantages of easy colorimetric tunability, wide field of view of the diffraction pattern visible to the eye, and rapid imprinting of uniform and low-cost sensors.

2.6. Relative Humidity Sensing

Development of sensors for visual indication of relative humidity (RH) in the environment is essential in industrial and domestic applications. The range of RH that is of interest for any specific application is different; thus, the sensitivity of the sensor needs to be optimized. To demonstrate the flexibility with which the initial appearance and the sensitivity of the nanoimprinted pyramidal structure to an analyte can be changed, a series of experiments were carried out. First, nanostepped pyramidal arrays with step size of 165, 180, and 195 nm were spin-coated with a poly(vinyl alcohol) (PVA) layer. The coating layer suppresses the diffraction from the low spatial frequency periodical structure (≈3.3 μm) and narrow-band diffraction was observed for different heights of the pyramidal steps (Figure 5e). The uncoated honeycomb array diffracted light due to the coexistence of two periodical structures created in holographic reflection and transmission modes. When the photonic structure was coated with a PVA layer, the refractive index modulation responsible for the diffraction from the transmission structure significantly decreased. Initially, the refractive index modulation was determined by the difference in the refractive indexes of air and the plastic substrate coated with an aluminum layer (≈20 μm). Spin-coating the nanosteps with PVA displaced the air and matched the surrounding refractive index close to the one of the plastic substrate. Thus, the efficiency of the transmission grating was diminished and the optical response of the device was predominantly determined by the nanosteps. This observation was consistent with the color of the diffracted light that depended on the nanostep height (Figure 5e).

The sensitivity of the sensor was optimized by changing the chemical composition of the coating layer. Aluminum side of the nanostepped pyramidal arrays with a step height of 175 nm were each coated with PVA/glycerol (1:0, 1:1, 2:3 wt%). The samples were placed in a controlled humidity chamber and were

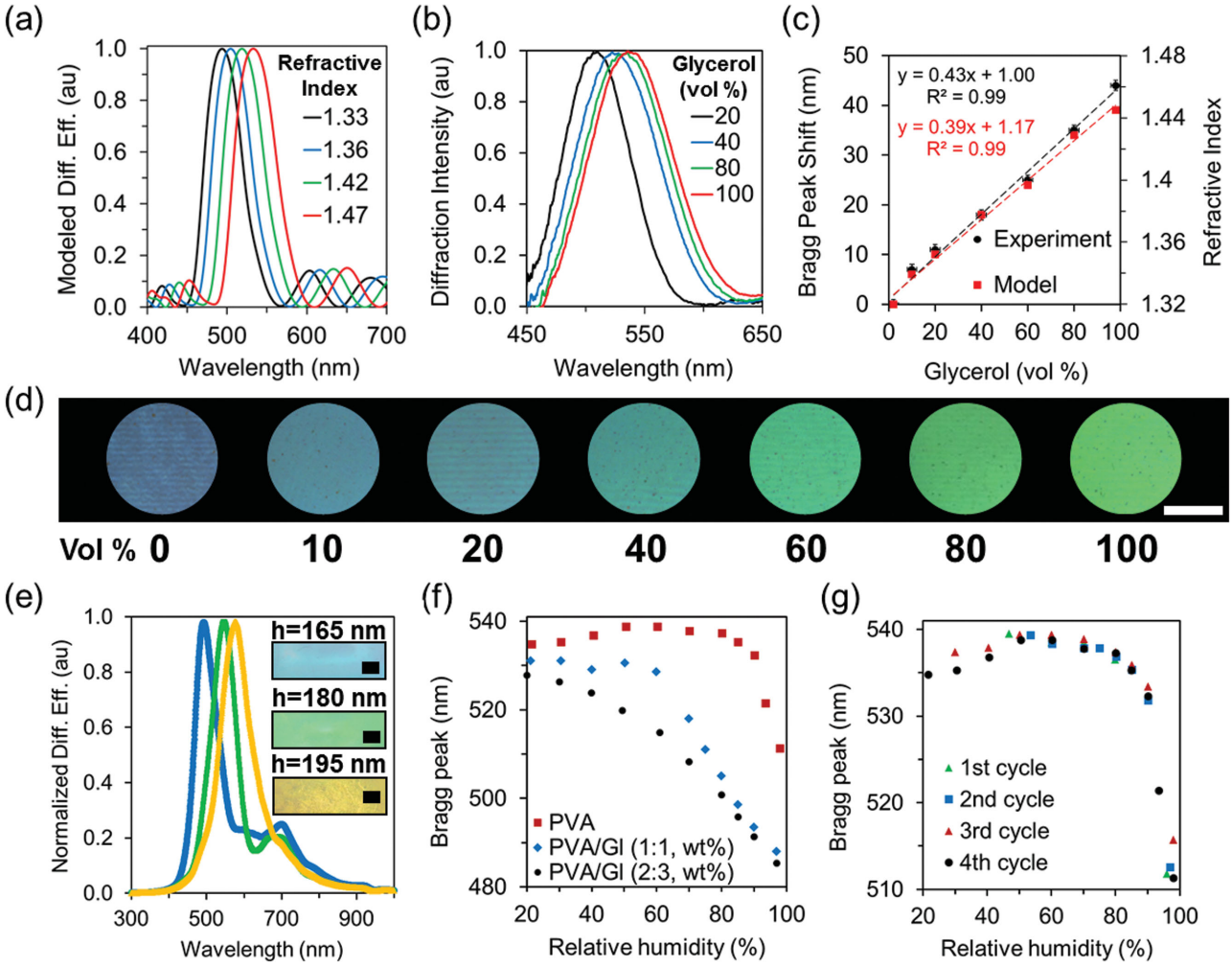

Figure 5. The applications of printable holographic 2.5D nanostepped Bragg gratings in sensors. a) Simulated finite element model showing Bragg peak shifts as a function of changes in external refractive index. b) Nanostepped pyramid refractive index sensor (h = 180 nm), showing 45 nm shift in the position Bragg peak as the concentration of glycerol was increased incrementally. c) Quantification of the glycerol concentration as a function of variation in refractive index of the surrounding medium (n = 10 for each measured sample). d) The colorimetric readouts of the refractive index sensor with changing glycerol concentration. Scale bar = 5 mm. e) Bragg peaks of PVA-coated gratings with different nanostep sizes. The inset shows the photographs of the PVA-coated gratings. Scale bar = 5 mm. f) The change in Bragg peak as the RH increases g) RH repeat cycles.

illuminated with a broad spectral range beam of light. Figure 5f shows the dependence of the peak wavelength of the diffracted light on the RH in the chamber. The addition of glycerol to the PVA solution spin-coated on top of the nanostepped pyramidal array structure increases the sensitivity of the sensor—particularly at the low RH range. The repeatability and the reversibility of the changes in devices coated with PVA and PVA/glycerol (1:1) layers were confirmed after exposure to RH above 90% (Figure 5g). The layer with composition of PVA/glycerol (2:3) is suitable for operation at lower RH. The presented RH sensors can be explored to create sensors operating at low RH region where the demand for highly sensitive devices in electronics, food, and pharmaceutical packaging is high.

2.7. Multilevel Security Labels

We also demonstrate the application of the holographic honeycomb nanostepped pyramids in printing multilevel security labels. Current standard for security labels is surface holograms, which diffract rainbow colors upon illumination with broadband light. Although volumetric 3D holograms can be created through silver halide chemistry or photopolymers (e.g., Polaroid DMP-128), may not meet cost requirements at high volume. Moreover, fake labels or patterns can be easily created to resemble genuine labels, and existing rainbow holograms offer limited protection against counterfeit products. For example, many reflective materials including silver foil copies, and convincing fake holograms have been found on counterfeit medicines.[32] Currently, there is a need to produce technically advanced verification mechanisms to prevent counterfeit medicines and high-value products. To create multilayer security labels, we created 2.5D holographic array assemblies using a photomask for Bragg gratings that diffract light at 500, 544, 599, and 620 nm, respectively (Experimental Section "Device Assembly"). **Figure 6**a illustrates an image of the dove used in credit cards. The photonic color-selective capability of the 2.5D

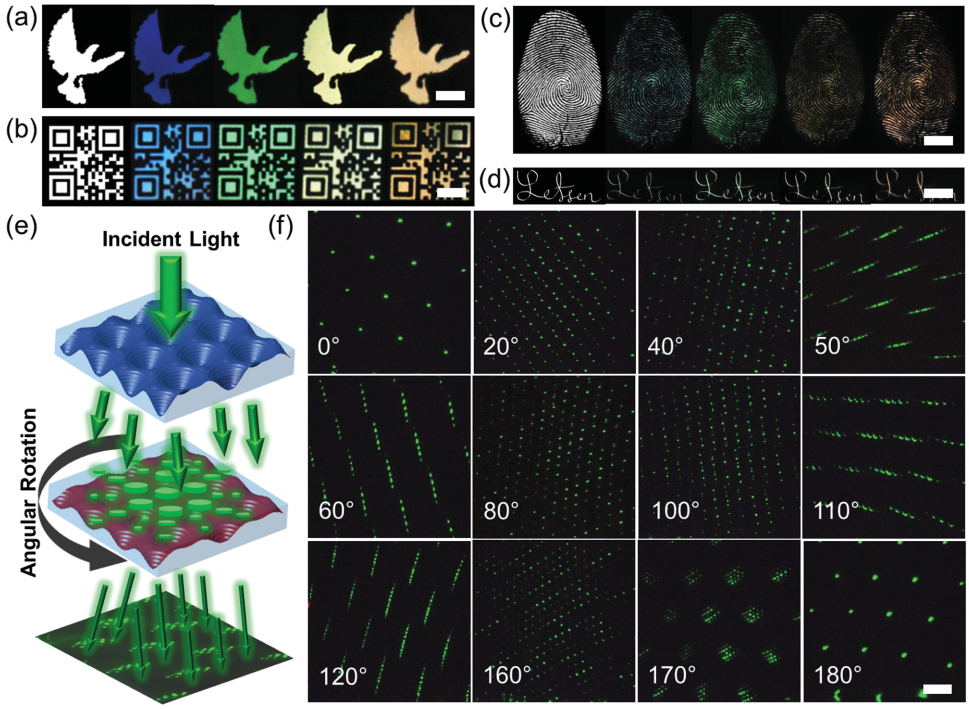

Figure 6. The applications of 2.5D holographic nanostepped Bragg gratings in multilevel security labels. a) Holographic dove as a security label. The gratings diffract light at 500, 544, 599, and 620 nm, corresponding to step sizes of 160, 180, 195, and 200 nm, photographed from the normal. Left column shows the masks. b) QR codes, c) fingerprints, d) handwritten signatures. (a–d) Scale bar = 5 mm. e) Experimental setup for creating overlapped far-fields using two Bragg gratings in transmission mode. f) Far-field images of nanostepped Bragg gratings at different angular rotation positions. Scale bar = 2 cm.

nanostructures can be utilized in the identification of counterfeit credit cards. We also prepared optically encryptioned QR codes to securely identify high-volume products for application in drug packages, blister cards, and capsules (Figure 6b). 2.5D nanostepped pyramids can be used in dactyloscopy to biometrically identify an individual, or placed on highly secure documents such as passports, identification documents, and polymer banknotes. For example, the holographic nanostepped pyramids can display prescanned fingerprints (Figure 6c). Human fingerprints are unique markers that are difficult to alter, and durable over the life of an individual. Figure 6d shows a handwritten signature for application in personalizing and authenticating autographs. The honeycomb 2.5D holographic arrays can be visually distinguished from rainbow (polychromatic) holograms and reflective foils since the present technology provides multilevel authentication of a product: (i) color-selective diffraction is easily verified, (ii) the array projects a far-field honeycomb pattern when illuminated with laser light, and (iii) the QR code can be decoded easily using a smartphone to rapidly authenticate a product.

Different patterns can be obtained at the far field by using two 2.5D holographic arrays with a relative angle between them. According to the convolution theorem, the effect observed at the far-field corresponds to the circular convolution of the two independent rotated holograms. This phenomenon can be observed when the holograms work in transmission mode. We have demonstrated this effect by superposing the two nanostepped pyramidal array holograms with a relative angle between them (Figure 6e). When the angle is zero, the autocorrelation of the hexagonal pattern is equivalent to another hexagonal pattern producing no observable effect of the convolution. However, when the second hologram is rotated, multiple diffractive spots emerge from the hexagonal pattern spots. Furthermore, these spots overlap at larger angles creating complex diffractive patterns. Figure 6f shows far-field images as the second hologram was rotated from its original position to 180°, showing distinct diffraction features (field distribution). This effect can be expanded by superposing multiple holographic diffraction patterns. 2.5D holograms act as a secure code analogous to space division multiplexing in the data communication systems. Additionally, 2.5D nanostructures can be combined with metasurface holograms with polarization functionalities, plasmonics, or graphene oxide gratings to enhance multilevel security.

3. Conclusions

We developed a top-down strategy to print holographic honeycomb arrays consisting of 2.5D nanostepped pyramids on flexible substrates. Our approach has many attractive attributes due to its flexibility for tuning the Bragg diffraction of the gratings, possibilities of customization for personal use, and compatibility with mass manufacturing. Predicted by the analytical models for modulating the incident angle (θ) during prism coupling and azimuthal angle (α) during off-axis interference, our fabrication approach allows for fine-tuning the optical characteristics of the gratings such as the position and the bandwidth of Bragg peak as well as its diffraction intensity based on the accurate

modulation of the geometry of the pyramids and the density of hexagonal packing. These 2.5D photonic structures can be printed on flexible substrates to have color-selectivity in the visible spectrum observed in an angular range of 20° from the normal. We also demonstrated the scalability of this technique by printing the nanostepped pyramids over large areas (1 m^2) in roll-to-roll manufacturing within a minute. The application of the nanostepped pyramids was demonstrated in quantitatively sensing refractive index. Our production strategy allows using a large variety of materials as film substrates, including transparent and opaque hydrophobic or hydrophilic polymers, with simple or complex geometries. Furthermore, using our technique, 2.5D nanostepped pyramids can be selectively patterned and multiplexed within a single device. Such information may be kept as proprietary information and used for the secure verification of high-value products and legal documents.

The ability to produce nanoscale color-selective gratings with large area on flexible substrate has broad applications. For example, these materials may find applications in solar cells, optical devices, tissue engineering, imaging, or photomedicine. In optics, they can be patterned as Fresnel lenses to focus monochromatic light in solar panels. Furthermore, they can be integrated with actuators based on electronics, heating, magnetism, or acoustics to tune the wavelength of the Bragg peak. These mechanisms may allow for creating tunable lasers. The surface of nanostepped pyramids can be functionalized with analyte-sensitive hydrogels to be selective to biomolecules such as pH, metal ions, glucose, proteins, and DNA.[33] The color of the diffracted light might be read to quantify the concentration of these analytes for application in microfluidic point-of-care diagnostics. For applications in tissue engineering, the nanostepped gratings can be used with hydrogels to map localized metabolite changes in scaffolds. Since the 2.5D gratings can be miniaturized, they might be integrated in fiber optics and waveguides for application in biomedical imaging techniques and photodynamic therapy.[34] We envision that 2.5D holographic honeycomb nanostepped pyramids can be integrated with desktop dot-matrix printers for rapidly producing devices in optics, security, and medicine.

4. Experimental Section

Electromagnetic Modeling of Nanosteps: The diffraction from the gratings was modeled using a finite element method based computational software, COMSOL Multiphysics. The model consisted of a 2D geometry of nanostepped pyramids with spacing on the order of 3 μm. The 2D simulated geometry represents the cross-section of the 2D pyramid array, taking advantage of the planar symmetry in the x-y plane. The pyramids were made from acrylate polymer (AP) (n = 1.49) coated with a 30 nm layer of aluminum on poly(ethylene terephthalate) (PET) (n = 1.57). The unit cell of the geometry consisted of two pyramids with periodic conditions placed across the edges. A hemispheral domain was placed on top of the grating layer, and the area within the hemisphere was defined as air. A broadband light source illuminated the grating normally from the top. The diffracted light was collected from the entrance of the light incident beam.

Holographic Writing of Nanostructures: The samples were fabricated and provided by Cowan[28] (Aztec Systems, Inc., Lexington, MA) and Slafer[28] (MicroContinuum, Inc., Cambridge, MA). The fabrication of the grating consisted of spin coating positive photoresist (diazonaphthoquinone) over a glass substrate (1.0 mm) at 100 rpm for 2 min. The photoresist was baked at 80 °C for 1 h, and it was patterned in two main steps: multilayer exposure (prism coupling) and opening exposure. First, 1/8 of the photoresist surface area, corresponding to a 1.5 cm wide stripe was left open and the rest of the photoresist was blocked with an opaque mask. Xylene (n = ≈1.50, 1 mL) was deposited over the glass substrate, and a triangular prism was placed over the glass substrate to match the refractive indexes. The contact was between the glass surface of the prism and the glass side of the photoresist coated plate. The photoresist side of this plate is exposed directly to air. In prism coupling, a laser beam (λ = 458 nm, 100 mW, Ø = 14 cm) deviated from a mirror mounted on top of an air bearing was scanned over the stripe at 10° from the normal of the prism surface plane for 1 min. This exposure step created a multilayer interference pattern due to total internal reflection in the photoresist–air interface. After the first exposure, the adjacent stripe region was opened and the other regions were masked, and the exposure was carried out at an incident angle of 16° from the normal of the prism surface plane. This process was repeated until the entire photoresist surface was exposed up to 50° incident beam. The last stripe was used as a blank control. In the second opening exposure step, the entire area of the photoresist layer from the SiO_2 side was exposed to three azimuthal beams (120°) (λ = 458 nm, 100 mW, Ø = 14 cm) for 1 min. This process results in hexagonally packed cylindrical interference fringes running normal to the photoresist surface plane. The photoresist was etched using a photographic developer.

Nanoimprint Lithography: To print the gratings, a master (inverse pattern) originally developed by Cowan (Aztec Systems, Inc.) was used.[27] The master protected the original photoresist by creating many working copies. A silver layer (≈300 nm) was evaporated over the photoresist in vacuum. The master was fabricated by electroplating metallic nickel over the patterned photoresist in a galvanic tank. The nickel master (t = 1 mm) consisted of convex stepped structures extruded from its surface plane. The nickel master was installed onto a cylindrical drum of a roller-type replication machine, and the grating was printed onto AP film (≈2 μm) on a PET substrate (≈100 μm) using UV-initiated nanoimprint lithography. To increase the diffraction efficiency of the convexities, an aluminum layer was coated by evaporation over the embossed AP film.

Scanning Electron Microscopy: Gratings from the aluminized AP-PET layer were cut to 2 × 2 mm size. The samples were mounted on a SEM aluminum stub. To image the concavities, Merlin (Zeiss) SEM was used at 1.5 kV with a working distance of 4.1×10^{-3} (cross-section) to 5.5×10^{-3} M (flat) coupled to Signal A: SE2 or InLens detector. Cross-sectional images were acquired from the surface plane of the gratings (90° sample holder).

Atomic Force Microscopy: AFM images were acquired using Cypher AFM (Asylum Research) in AC/tapping mode using an arrow UHF silicon probe (NanoWorld, Asylum Research).

Nanostructure Assembly: Black opaque masks were printed on a cellulose acetate transparency film (Staples, 21.6 × 27.9 cm, t = 0.1 mm) using a laserjet printer (HP, CP2025). Image colors were inversed before printing. The masks were assembled on the AP side of the gratings. Masks could be used to block light during laser exposure, or the patterns can also be created using CO_2 laser cutting.

Optical Characterization: The gratings were cut to 1 × 1 cm^2 square samples and assembled on a robotic rotation mount (Thorlabs) with 360° continuous rotation. A 3 mm spot on the PET surface of the gratings was illuminated at normal incidence with an ultraviolet-visible-near infrared light source (Ocean Optics, DH-2000). The back-scattered spectra was collected at 1° increments from 0° to 60° relative to the sample normal using a reflection spectrometer (Ocean Optics, Maya Pro-2000) positioned on a robotic goniometer controlled by IGOR Pro (v6.3, Wavemetrics). The spectra of the incident light (blank) was recorded by reflecting it from a plane mirror and the diffraction spectra was divided by blank spectra. The intensities of the resulting spectra were normalized to 1.0.

The spectra of the Bragg peaks were measured using an optical fiber coupled into a port of an upright optical microscope (Olympus).

Broadband light was used to illuminate the PET side of the gratings normal to the surface plane, and the backscatter was collected from the illumination direction. The spectra of the incident light (blank) was recorded, and the diffraction spectra was divided by blank spectra. The intensities of the resulting spectra were normalized to 1.0.

The hemisphere was fabricated by cutting a semitransparent white plastic ball (Ø = 4 cm) in two halves and drilling a 3 mm hole on top of the hemisphere. The gratings from the PET surface side were illuminated normally with an optical fiber (Thorlabs, M13L01 – Ø400 µm, 0.39 NA, 1 m) connected to NCL 150 (Volpi, 20 V/150 W) broadband cold light halogen lamp. Monochromatic illumination of the gratings was achieved using a continuous wave laser pointer (λ = 532 nm, 1 mW, spot Ø = 1 mm). Photographs of the gratings from the PET surface side were captured by a digital single-lens reflex camera (Nikon D90, 12.3 MP) using a Nikkor lens (Nikon, AF-S DX 18–105 mm f/3.5-5.6G ED VR).

Diffraction efficiency measurements were carried out by normally illuminating the gratings with a green-blue laser (Cobolt Dual Calypso, Class 3B, 491/532 nm, 100 mW) and red laser (Coherent Cube, 640 nm, 40 mW). The diffracted light was measured both in reflection and transmission modes using a powermeter (Newport, 1918-R). Far-field diffraction measurements of angularly convoluted gratings without Al coating were carried out using a rotation mount. The stationary hologram was fixed on one side of the mount and the other hologram was assembled on the rotating side. The hologram was illuminated with laser light (λ = 532 nm, 1 mW). A black screen 15 cm away from the rotating hologram was used to project the far-field diffracted light.

Refractive Index Sensing: Glycerol stock solutions were prepared from 10 to 90 vol% in water. The glycerol sample (100 µL) was deposited over gratings (1 cm^2) and a cover slip was placed on top. The diffracted light was collected using an upright optical microscope. New gratings were used for each measurement.

Relative Humidity Sensing: Nanostepped pyramidal structures with a step height of 175 nm were spin coated with different solutions containing PVA/glycerol in different ratios (1:0, 1:1, 2:3 wt%). The structures were studied in a controlled humidity and temperature environment (Electro-tech Systems, Inc. Model 5503–11). The RH in the chamber was maintained to ±1% RH of the set point in an operational range 5%–100% RH. The temperature in the chamber was maintained at 21 ± 1 °C. The optical setup for measuring the spectral characteristics of the light diffracted from the hologram was assembled in the environmental chamber. The probe light from a broadband light source (AvaLight-HAL-S, Avantes) was fiber guided into the humidity chamber. The diffracted light was then coupled into a second fiber by a lens and guided to a spectral analyzer (AvaSpec-2048, Avantes). To obtain the humidity response of a specific grating, the correlation between the peak wavelength of the light diffracted from the nanostepped array and the RH was determined.

Supporting Information

Supporting Information is available from the Wiley Online Library or from the author.

Acknowledgements

This work was supported by the Leverhulme Trust (RF-2016-039) and the Wellcome Trust (201929/Z/16/Z). The authors acknowledge James J. Cowan and W. Dennis Slafer for fabricating the gratings used in this study and discussions on fabrication. The authors thank Jeff Blyth for discussions. The authors also thank Grant England, Elijah Shirman, Ida Pavlichenko, Joanna Aizenberg, B. V. Lotsch, and Viola D. for angular measurements, SEM and AFM imaging. Author Contributions: A.K.Y. designed the project and wrote the article. A.K.Y., T.M., and M.H. performed the experiments. H.B., R.A., and Y.M. carried out the simulations. A.Y., H.B., R.A., I.N, and S.M. analyzed the data and revised the article. The authors declare no competing financial interests.

Received: March 9, 2016
Revised: April 26, 2016
Published online: July 5, 2016

[1] J. Ge, Y. Yin, *Angew. Chem. Int. Ed.* **2011**, *50*, 1492.
[2] a) D. E. Smalley, Q. Y. J. Smithwick, V. M. Bove, J. Barabas, S. Jolly, *Nature* **2013**, *498*, 313; b) C. Fenzl, T. Hirsch, O. S. Wolfbeis, *Angew. Chem. Int. Ed.* **2014**, *53*, 3318.
[3] a) A. Llordés, G. Garcia, J. Gazquez, D. J. Milliron, *Nature* **2013**, *500*, 323; b) G. England, M. Kolle, P. Kim, M. Khan, P. Muñoz, E. Mazur, J. Aizenberg, *Proc. Natl. Acad. Sci. USA* **2014**, *111*, 15630; c) M. Schaffner, G. England, M. Kolle, J. Aizenberg, N. Vogel, *Small* **2015**, *11*, 4334.
[4] G. Bazin, X. X. Zhu, *Prog. Polym. Sci.* **2013**, *38*, 406.
[5] C. I. Aguirre, E. Reguera, A. Stein, *Adv. Funct. Mater.* **2010**, *20*, 2565.
[6] F. H. Schacher, P. A. Rupar, I. Manners, *Angew. Chem. Int. Ed.* **2012**, *51*, 7898.
[7] D. Schneider, F. Liaqat, E. H. El Boudouti, Y. El Hassouani, B. Djafari-Rouhani, W. Tremel, H.-J. R. Butt, G. Fytas, *Nano Lett.* **2012**, *12*, 3101.
[8] a) J. F. Galisteo-López, M. Ibisate, R. Sapienza, L. S. Froufe-Pérez, Á. Blanco, C. López, *Adv. Mater.* **2011**, *23*, 30; b) G. von Freymann, V. Kitaev, B. V. Lotsch, G. A. Ozin, *Chem. Soc. Rev.* **2013**, *42*, 2528.
[9] L. Feng, Y.-L. Xu, W. S. Fegadolli, M.-H. Lu, J. E. Oliveira, V. R. Almeida, Y.-F. Chen, A. Scherer, *Nat. Mater.* **2013**, *12*, 108.
[10] W. Luo, J. L. Kou, Y. Chen, F. Xu, Y. Q. Lu, *Appl. Phys. Lett.* **2012**, *101*, 133502.
[11] S. Takahashi, M. Okano, M. Imada, S. Noda, *Appl. Phys. Lett.* **2006**, *89*, 123106.
[12] S. Wong, M. Deubel, F. Pérez-Willard, S. John, G. A. Ozin, M. Wegener, G. von Freymann, *Adv. Mater.* **2006**, *18*, 265.
[13] a) J. Fleming, S. Lin, I. El-Kady, R. Biswas, K. Ho, *Nature* **2002**, *417*, 52; b) A. Blanco, E. Chomski, S. Grabtchak, M. Ibisate, S. John, S. W. Leonard, C. Lopez, F. Meseguer, H. Miguez, J. P. Mondia, *Nature* **2000**, *405*, 437; c) N. Tétreault, G. von Freymann, M. Deubel, M. Hermatschweiler, F. Perez-Willard, S. John, M. Wegener, G. A. Ozin, *Adv. Mater.* **2006**, *18*, 457.
[14] S. Matthias, F. Müller, C. Jamois, R. B. Wehrspohn, U. Gösele, *Adv. Mater.* **2004**, *16*, 2166.
[15] G. von Freymann, A. Ledermann, M. Thiel, I. Staude, S. Essig, K. Busch, M. Wegener, *Adv. Funct. Mater.* **2010**, *20*, 1038.
[16] P. Viktorovitch, B. Ben Bakir, S. Boutami, J. L. Leclercq, X. Letartre, P. Rojo-Romeo, C. Seassal, M. Zussy, L. Di Cioccio, J. M. Fedeli, *Laser Photonics Rev.* **2010**, *4*, 401.
[17] R. Peretti, C. Seassal, P. Viktorovich, X. Letartre, *J. Appl. Phys.* **2014**, *116*, 023107.
[18] B. Ben Bakir, C. Seassal, X. Letartre, P. Regreny, M. Gendry, P. Viktorovitch, M. Zussy, L. Di Cioccio, J.-M. Fedeli, *Opt. Express.* **2006**, *14*, 9269.
[19] Y. N. Denisyuk, *Dokl. Akad. Nauk SSSR* **1962**, *144*, 1275.
[20] a) S. A. Benton, V. M. Bove, *Holographic Imaging*, John Wiley & Sons, Hoboken, NJ **2007**, p. 173; b) B. J. Chang, C. D. Leonard, *Appl. Opt.* **1979**, *18*, 2407.
[21] C. P. Tsangarides, A. K. Yetisen, F. D. Vasconcellos, Y. Montelongo, M. M. Qasim, T. D. Wilkinson, C. R. Lowe, H. Butt, *RSC Adv.* **2014**, *4*, 10454.
[22] a) P. N. Tamura, *Appl. Opt.* **1978**, *17*, 2532; b) J. L. Walker, S. A. Benton, *Proc. SPIE* **1989**, *1051*, 192.
[23] E. N. Leith, J. Upatnieks, *J. Opt. Soc. Am.* **1962**, *52*, 1123.
[24] S. A. Benton, *US Patent 3,633,989 A*, **1972**.

[25] J. J. Cowan, *J. Opt. Soc. Am. A* **1990**, *7*, 1529.
[26] S. H. Ahn, L. J. Guo, *ACS Nano* **2009**, *3*, 2304.
[27] J. J. Cowan, presented at *Proc. Int. Conf. on Holography*, Wales, UK, July **2006**.
[28] a) J. J. Cowan, *Opt. Eng.* **1985**, *24*, 245796; b) J. J. Cowan, W. Slafer, *Imaging Sci. J.* **1987**, *31*, 100; c) M. Ozaki, J.-I. Kato, S. Kawata, *Science* **2011**, *332*, 218.
[29] N. S. King, L. Liu, X. Yang, B. Cerjan, H. O. Everitt, P. Nordlander, N. J. Halas, *ACS Nano* **2015**, *9*, 10628.
[30] J. Walia, N. Dhindsa, M. Khorasaninejad, S. S. Saini, *Small* **2014**, *10*, 144.
[31] Y. Dou, J. Han, T. Wang, M. Wei, D. G. Evans, X. Duan, *J. Mater. Chem.* **2012**, *22*, 14001.
[32] P. Aldhous, *Nature* **2005**, *434*, 132.
[33] A. K. Yetisen, I. Naydenova, F. da Cruz Vasconcellos, J. Blyth, C. R. Lowe, *Chem. Rev.* **2014**, *114*, 10654.
[34] D. Yelin, I. Rizvi, W. M. White, J. T. Motz, T. Hasan, B. E. Bouma, G. J. Tearney, *Nature* **2006**, *443*, 765.